

Ship Size Extraction for Sentinel-1 Images Based on Dual-Polarization Fusion and Nonlinear Regression: Push Error Under One Pixel

Boying Li, *Student Member, IEEE*, Bin Liu^{ID}, Weiwei Guo^{ID}, Zenghui Zhang, *Member, IEEE*, and Wexian Yu^{ID}

Abstract—In this paper, we present a method of ship size extraction for Sentinel-1 synthetic aperture radar (SAR) images, which is composed of the image processing stage and the regression stage. In order to achieve extraction with high accuracy, considering the data characteristics of Sentinel-1 images, we propose to use the dual-polarization fusion and the nonlinear regression with the gradient boosting. The experiments and analyses on a relatively large data set show that: 1) compared with the existing and related studies, the proposed method achieves an improved performance. The extraction errors are pushed under one pixel, and they are 4.66% (8.80 m) and 7.01% (2.17 m) for length and width, respectively; 2) the dual-polarization information fusion does improve the size extraction accuracy; and 3) the nonlinear regression does exploit the relationship between the influential factors and the size parameters and provide a better performance than the linear regression. The experimental results verify that the proposed design is suitable for ship size extraction in Sentinel-1 SAR images.

Index Terms—Dual-polarization fusion, nonlinear regression, Sentinel-1, ship size extraction, synthetic aperture radar (SAR) image.

I. INTRODUCTION

IN RECENT years, the role of satellite synthetic aperture radar (SAR) data in marine surveillance has become more and more remarkable. Sentinel-1 is a space mission of SAR in C-band carried out by the European Space Agency. Its capability of providing wide coverage and medium-to-high resolution [1] products under all weather makes it a well-suited data resource for global marine surveillance. Based on this publicly available data set, studies have been carried out and its usefulness has been proven in many fields, such as ship detection and classification, iceberg detection, wind retrieval, oil spill detection, sea ice surveillance, and ship wake detection [2]–[9]. Size extraction can be regarded as the basic and key issue to marine target detection and classification. The

Manuscript received November 28, 2017; revised March 30, 2018; accepted April 27, 2018. Date of publication June 21, 2018; date of current version July 20, 2018. This work was supported by the National Natural Science Foundation of China through the State Key Program under Grant 61331015. (*Corresponding author: Bin Liu*.)

B. Li, W. Guo, Z. Zhang, and W. Yu are with the Shanghai Key Laboratory of Intelligent Sensing and Recognition, Shanghai Jiao Tong University, Shanghai 200240, China.

B. Liu is with the College of Marine Sciences, Shanghai Ocean University, Shanghai 201306, China (e-mail: liubin22810@gmail.com).

Color versions of one or more of the figures in this paper are available online at <http://ieeexplore.ieee.org>.

Digital Object Identifier 10.1109/TGRS.2018.2841882

elaborate geometric parameter estimation is essential to SAR imagery interpretation. Hence, geometric parameter extraction with high accuracy based on Sentinel-1 products is a very crucial and meaningful task for marine surveillance.

In general, metallic objects, such as ships, are clearly perceived on SAR signatures, because they can reflect the electromagnetic waves strongly, in contrast to the water surrounding them [10]. Under the medium resolution condition, the backscattering in the SAR signature can be regarded as the contribution of multiple scatterers, including the ship superstructure, the environment, and the sea–ship interaction. On one hand, SAR images contain rich information about marine targets. On the other hand, due to the typical imaging mechanism of SAR systems, multiple factors have influences on the SAR signatures. The side-look geometry, the wavelength influence, the sidelobe effect, the resolution limitation, the smearing effect induced by movement, and so on may worsen the image quality as well as bring ambiguities in the size estimation. Insufficient or oversimplified consideration of these effects as well as the inner relationships of factors would limit the performance improvement of the ship size extraction.

Focusing on Sentinel-1 products, research has been carried out to analyze the aforementioned factors. The relationship among the incidence, the polarization, the selected mode, and the environment in marine target detection has been analyzed [9]. The impacts of different electromagnetic wavelengths, resolutions, polarizations, and radar illumination geometries have been analyzed by comparison with TerraSAR-X products [7], [11]. Considering the wind information additionally, the sensor performances have been deeply analyzed [12].

Size extraction with high accuracy needs to overcome undesirable effects among the aforementioned factors. Aiming to get accurate size parameters, an extraction procedure generally includes three main stages: 1) binarization; 2) image operations for accurate size extraction; and 3) elaborate geometric parameter estimation. The first stage refers to the processing of dividing pixels into two classes: target and nontarget. Studies developed various detection methods [13]–[15] or fused different detection methods [16] to improve the detection performance and the size extraction performance simultaneously. The second and the third stages move forward based on the former results to get the estimation with high accuracy generally from two aspects: image operation and statistical

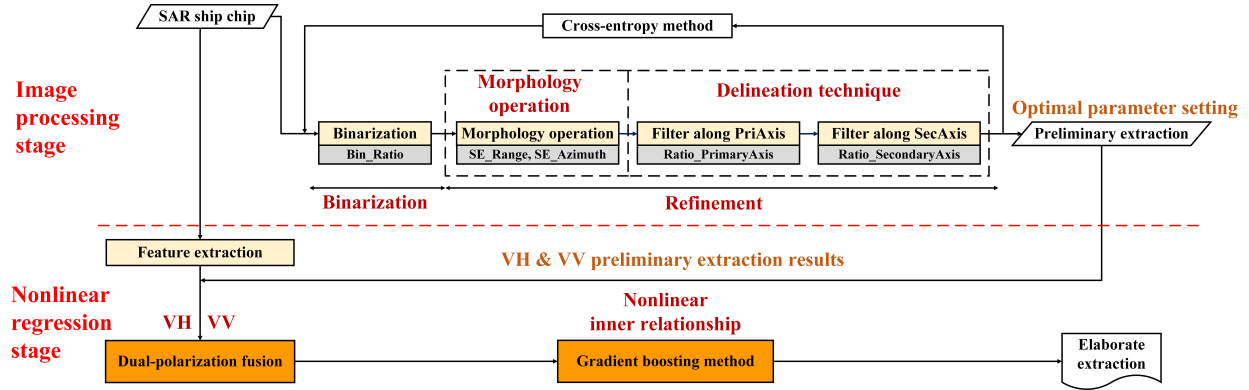


Fig. 1. Flowchart of the proposed size extraction method. The contributions are emphasized in the orange rectangles.

refinement. Image operation, such as the mathematical morphology processing [17], has been employed in the Sentinel-1 data set containing 127 samples to extract ship length and width, and the result mean errors are 16% (30 m) and 37% (11 m) for the length and width estimations, respectively. Statistical parameter refinement approaches by taking scattering information into consideration, such as the statistical model methods [18]–[20], the regression method [21], and the fuzzy method [22], are used for accurate size parameter estimation.

Though the aforementioned studies achieve good performances, several issues still exist: 1) to analyze and test the performance on a large-volume data set under various circumstances; 2) to exploit the dual-polarization information of Sentinel-1; and 3) to study the inner relationships among influential factors and size parameters and to explore more suitable models. The performance of size extraction can be further improved by addressing these issues. Therefore, in this paper, based on the OpenSARShip [23], a large-volume data set dedicated to Sentinel-1 ship interpretation, we fuse the dual-polarization information and exploit the nonlinear inner relationships among influential factors and size parameters in the regression model. The proposed method for size parameter extraction achieves a better performance and pushes the extraction error under one pixel size. Based on the relatively large and diverse data set, we test and analyze the performance. Furthermore, the performance is confirmed in another data set with different environmental conditions, indicating the applicability and the generalization ability of the model presented in this paper. Sufficient experiments ensure the availability and the robustness of this method from diverse aspects.

Considering that the interferometric wide-swath (IW) mode with VV + VH (vertical emitting and vertical and horizontal receiving, respectively) polarizations is the default mode over land/harbors [24], the exploration of the dual-polarization utilization in the Sentinel-1 data set is meaningful. In addition, according to many efforts to study the statistical ship models [18]–[20], the established regression model based on the nonlinear inner relationship assumption should be a reasonable solution. In this paper, the method of the dual-polarization fusion and the nonlinear regression with the gradient boosting is proposed and convincing results are obtained.

The remainder of this paper is organized as follows. Section II analyzes the multiple factors influencing the SAR

signatures and introduces the proposed method for size extraction. In Section III, the experimental results are presented and analyzed. Section IV gives the conclusions.

II. METHOD

The whole flowchart of the proposed size extraction is shown in Fig. 1. Motivated by [17] and [21], the procedure is mainly composed of two stages: image processing and nonlinear regression. The former stage delineates the ship contour close to one-pixel accuracy. Parameters used in this stage are optimized via the cross-entropy method. In the second stage, the information from two polarization modes is fused. Next, the regression model based on the nonlinear inner relationship assumption is established. This stage further improves the preliminary result and pushes the extraction error under one pixel.

In this section, the method is described in this order: first, we introduce the factors that are influential to the size extraction as the basis for this paper; then, the image processing part is presented; and finally, we describe the dual-polarization information fusion and the nonlinear regression.

A. Main Influential Factors

Multiple factors have impacts on the geometric parameter extraction. This section introduces these factors and their influences and provides guidance to the whole procedure design. Due to the typical imaging mechanism of the SAR system, the factors and their influences are introduced from the following three aspects.

1) *Sensor*: The multiple parameters [24] of the SAR system, such as resolution, polarization, and frequency, have essential influences on the SAR products. In addition, other factors, such as the number of looks, the processing on products, and the sidelobe, also impact the SAR signatures. Focusing on Sentinel-1, a spaceborne SAR system, the parameters of the satellite can also impact the products, such as the orbit height and the inclination of the satellite. Here, we only select relatively more important factors to analyze.

1) *Resolution and Processing on Products*: Spatial resolution limits the SAR image interpretation. From the basic point target assumption [25], scatterers can be regarded as a group of independent ideal point targets.

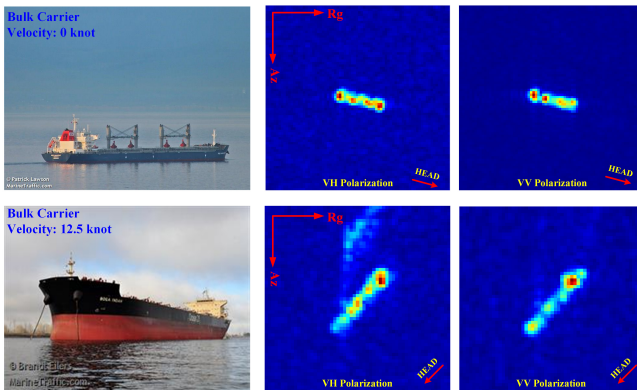


Fig. 2. Impacts of movement and polarization on the ship signatures. Visually, the impact of movement is more remarkable in the VH polarization.

Considering the medium resolution (20 m for the main marine surveillance products) of Sentinel-1 products, a single resolution unit contains a large number of point targets. The mixture of reflections of various scatterers in one single resolution unit, such as the environment and the target, brings ambiguities to geometric parameter extraction in SAR images.

The processing on products also has influences on SAR signatures. The ground range detected (GRD) products [24] consist of focused SAR data, which are multilooked and projected to ground range together with the speckle reduction. Some of the above operations, such as the multilooking, may bring ambiguities to SAR signatures and adverse effects on the size extraction.

- 2) **Polarization:** For one marine target, different polarizations have distinctive signatures and contain dissimilar information. In this paper, we focus on the polarization combination of VH and VV in the IW mode, because this combination is the default mode for land monitoring, especially in harbor regions where numerous ships locate. VH indicates the channel of transmitting vertically and receiving horizontally polarized signals, and VV indicates the channel of transmitting and receiving both vertically polarized signals. Various studies have been conducted in this direction. First, according to [7], the VH polarization is generally more sensitive to the volume scattering than the direct and the double-bounce scattering. Second, according to [2], the VV polarization provides observations with higher clutter-to-noise ratio, and the observations with the VH polarization are more likely to be influenced by the system noise. Third, the reactions toward velocity are different in the VH and VV polarizations, as shown in Fig. 2. The first and second rows in Fig. 2 show the stationary and the moving ship chips, respectively. Comparing the ship signatures in the VH and VV polarizations, the observation that the movement impact is more noticeable in the VH polarization can be made. Finally, the sea clutter is more restrained in the VH polarization compared with the VV polarization.

Based on the existing analyses, the two polarizations have various characteristics, and under some

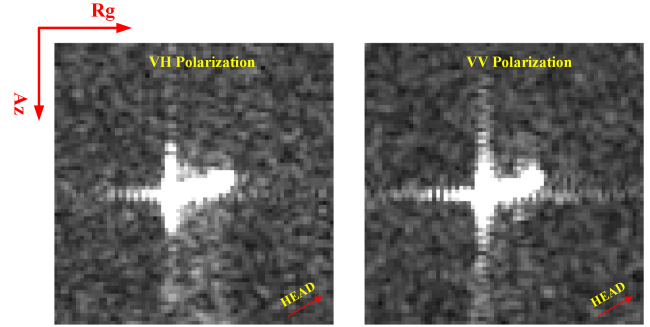


Fig. 3. Impacts of sidelobe on ship signatures.

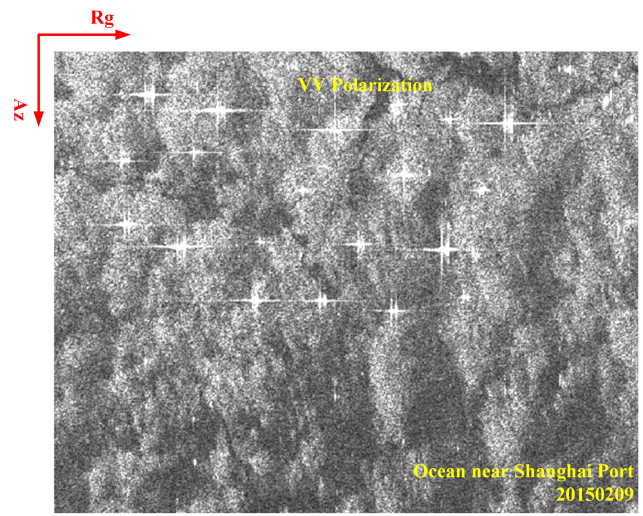


Fig. 4. Impacts of environment in the SAR imagery.

circumstances, they are mutually complementary. Taking the information of the dual-polarization mode together can improve the extraction performance.

- 3) **Sidelobe:** The SAR system forms a 2-D sinc(\cdot) function representation [26] of a scatterer, which may bring the following effects: 1) for the scatterer itself, the energy is dispersed at the center of scatterer, which causes the reduce of the intensity and the resolution of the scatterer and 2) for the regions surrounding the center scatterer, energy from the center may mask these regions, which brings confusion in SAR image interpretation. The phenomenon in SAR images, as shown in Fig. 3, is that the strong sidelobe appears as a bright cross along the range and azimuth directions surrounding the scattering center.
- 2) **Environment:** Some of the features in SAR images are related to the typical maritime environment [16], such as wind fronts, ocean waves, and rain cells. Fig. 4 shows an example of the sea clutter's impact on SAR imagery. The reflection of sea environment may induce the following problems. On one hand, the aforementioned factors make the statistical modeling of the sea clutter regions difficult. On the other hand, the sea-ship interaction brings several effects to the target. Some research [27]–[29] focuses on this topic via analyzing simulated and real products. The sea-ship interaction refers to the

interaction between the ship target and the sea environment. This interaction brings out a complex ship motion in the real world [27]–[29] and relatively different polarimetric scattering mechanisms [27], [28] in the SAR signature.

3) *Target*: The influential factors relating to the target are mostly the scattering signature of the ship hull and the target motion.

1) *Ship Hull*: The SAR images contain rich information about the ship targets, such as geometries, materials, and structures. In order to figure out the mapping between the SAR signatures and the ship structures in real world, several studies have been done [28]–[30]. The ship superstructure generally brings the following scattering mechanisms [7]: direct, double-bounce, volume scattering, and their mixtures considering the resolution limitation.

2) *Motion*: The target motion affects the SAR signature. The SAR system achieves its high resolution in the azimuth direction by the Doppler signal from the scatterer. For the stationary target, the azimuth position is assigned to be the azimuth position of the SAR platform. However, for the moving target, with a radial velocity component u , there is an additional component to the Doppler shift [31]. As the result, there is an azimuth displacement $d = (R/V)u$, where R denotes the distance between the SAR platform and the target and V denotes the velocity of the SAR platform. Another effect for the moving target is the image smearing. The nonstationary target point is often located in more than one resolution cell during the SAR integration time, and the dispersion of the backscattered energy causes the smearing and the degradation of brightness in the SAR image.

Consider the ship with six degrees of freedom, i.e., translation along three axes, pitch, yaw, and roll. The mixed motion, caused by the ship itself and the sea–ship interaction, brings smearing, distortion, and displacement in the SAR signature. According to the simulation in [29], different rotation movements together with cruising cause various effects, such as translation, rotation, scaling, and shearing in the relatively high resolution product, which are verified in TerraSAR-X images. Fig. 2 shows an example of target movement effects in Sentinel-1 images.

B. Image Processing

In this section, the image processing in the proposed method for geometric parameter extraction is introduced in detail. This stage includes the binarization operation and the further refinement operation based on the preliminary binary result. The former operation aims to retrieve rough ship regions by a uniform operation on the whole data set, and the latter one aims to remove noise pixels to get refined ship contours. The combination of the above two operations reduces the undesirable effects described in Section II-A to a large degree and delineates the geometric shape as the preliminary extraction

result. This is illustrated as the top half part of the flowchart in Fig. 1.

The preliminary extraction performance is determined by the design of the image processing stage as well as the parameters in this stage. The suitable parameters facilitate the precise delineation of the ship contour. In order to take the advantage of the samples with ground truth, motivated by [21] and [32], the image processing parameters are optimized by the cross-entropy method, a machine learning approach within the field of the Monte Carlo combinatorial optimization described in this section.

1) *Binariization*: For binarization, there are several conventional methods, such as the constant false alarm rate (CFAR) method. Here, the employed binarization operation is composed of preprocessing and threshold calculation. The intensity information of the SAR image is interfered by the multiplicative noise [33], i.e., if the signal is stronger, the variation of the intensity value is stronger, and if the signal is weaker, the variation is weaker. The preprocessing uses the log transformation to transform the multiplicative noise to additive noise and compress the data range for the higher values to facilitate the threshold calculation.

After the preprocessing, the binarization threshold calculation for one ship chip is described as follows:

$$I_{\text{th}} = \rho_{\text{th}}(I_{\max} - I_{\min}) + I_{\min} \quad (1)$$

$$I_{\text{mask}}(x, y) = \begin{cases} 1 & I(x, y) \geq I_{\text{th}} \\ 0 & I(x, y) < I_{\text{th}} \end{cases} \quad (2)$$

where $I(x, y)$ and $I_{\text{mask}}(x, y)$ denote the image values at the position (x, y) of the image after the preprocessing and the image after the binarization, respectively, I_{\max} and I_{\min} denote the maximum and the minimum values of I , respectively, I_{th} denotes the threshold for binarization, and ρ_{th} is the ratio for binarization and a parameter needed to be optimized by the cross-entropy method.

The CFAR is an option for the binarization, but it is worth noting that its performance is determined by two crucial factors: the suitable statistical model [34], [35] and the reasonable predefined false alarm value. Various scenes may have dissimilar suitable models. Considering that the images in practical use are acquired from a variety of scenes globally, the statistic model selection can be very complex. Therefore, to simplify the problem as well as to guarantee the performance, the above-described binarization operator is applied. In addition, the machine learning approach optimizes the parameter selection and improves the adaptability of this operator for various regions.

2) *Refinement of the Binary Result*: Following the binarization, the further refinement of the binary result is applied to reduce the undesirable effects, as shown in the rectangles with dotted-line frames in Fig. 1. First, we use the erosion and dilation morphology operations along the azimuth and range directions separately to reduce the sidelobe effect. Second, the delineation technique is employed, and it refers to the filtering that is performed three times, twice along the primary axis and once along the secondary axis. Here, the primary axis refers to the bow-stern axis, i.e., the axis of the length

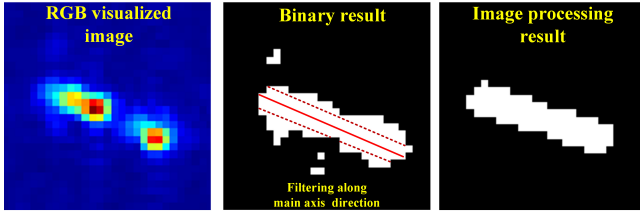


Fig. 5. Illustration of the filtering along the primary axis.

direction, and the secondary axis refers to the port-starboard axis, i.e., the axis of the width direction.

Here, we focus on the parameters employed in the above operations. For the morphology operations, we use the same line-shaped structure element in erosion and dilation for one direction. The sizes of these structure elements are set to s_{rg} and s_{az} for the range and azimuth directions, respectively, and they are needed to be optimized by the cross-entropy method.

In the filtering operation, we use the line masks along the primary and secondary axes to erase noise pixels. Taking the primary axis direction for example, as shown in Fig. 5, the red line represents the extracted primary axis. The dotted line represents the extracted line that is located in the ship region and parallel to the primary axis. Specifically, the dotted line is extracted as follows. First, from the binarized ship signature, the centroid and the primary and secondary axes can be extracted. Second, all the lines parallel to the extracted primary axis and across through the secondary axis are extracted.

The lengths of the primary axis and the extracted line are denoted as L_{PA} and L_{line} , respectively. If $L_{line} < \rho_{PA} L_{PA}$, all pixels in the extracted line are regarded as noise points and then erased. This is performed similarly in the secondary axis direction. If $L_{line} < \rho_{SA} L_{SA}$, where L_{SA} denotes the length of the secondary axis, the line pixels are erased. For the two directions, the two parameters, ρ_{PA} and ρ_{SA} , are the criteria for erasing noise points, and they are needed to be optimized by the cross-entropy method.

3) Optimization of the Parameter Selection: The number of parameters and their various ranges make the manual optimization very difficult; hence, it is necessary to optimize the parameter selection automatically.

In order to choose an optimal parameter setting automatically and take advantage of the data set with ground truth, the cross-entropy method [32] is utilized. Based on the Monte Carlo simulation, the cross-entropy method is a generic approach to combinatorial and multiextremal optimization. This technique [36] has been successfully applied to a wide range of discrete and continuous optimization tasks for deterministic and noisy problems.

The cross-entropy method is used to optimize the parameter selection for the image processing stage. Each parameter in the stage is adjusted dynamically and converges to the optimal choice. In general, the cross-entropy method contains two phases: generating a sample of random data based on a specific random mechanism and updating the parameters on the basis of a certain scheme. The cross-entropy method is described as follows for a full understanding of the proposed method.

- 1) The two variables, μ_i^p and σ_i^p , determine the distribution of each parameter in the procedure of optimization. μ and σ are the expectation and the standard deviation of the Gaussian distribution, respectively, the subscript denotes the i th iteration, and the superscript p denotes the p th parameter in the optimization. According to [21] and [37], the initial values μ_i^p and σ_i^p ($i = 0$) for every parameter are acquired from experience and experiments to guarantee the optimization performance.
- 2) Based on μ_i^p and σ_i^p , the Gaussian distribution is established and we get N parameter sets from the distribution. In this paper, N is set to 50, which ensures that the parameter arrangement is large enough.
- 3) Each parameter setting is applied in the image processing stage and evaluated by the evaluation function. The evaluation function is defined as

$$P(\hat{L}, L; \hat{W}, W) = \omega_L \frac{1}{M} \sum_{j=1}^M (\hat{L}(j) - L(j))^2 + \omega_W \frac{1}{M} \sum_{j=1}^M (\hat{W}(j) - W(j))^2 \quad (3)$$

where $\hat{L}(j)$ and $\hat{W}(j)$ are the measured length and width for the j th sample in each image processing iteration, respectively, $L(j)$ and $W(j)$ are their respective true length and width from the automatic identification system (AIS) information, M is the number of samples, and ω_L and ω_W are the weights to balance the influences of the errors in the length and width extractions in the evaluation function, respectively. In this paper, ω_L and ω_W are set to 0.55 and 0.45, respectively. In general, there are more ambiguities and higher errors in the width estimation, and thus, the error of the width estimation naturally contributes more in the evaluation. Hence, the evaluation function is slightly unbalanced in favor of length.

- 4) ρN elite samples that have the best performance according to the evaluation function in one iteration are drawn from the parameter sets to update μ and σ . The updating function is defined as

$$\mu_{i+1}^p = (1 - \alpha)\mu_i^p + \alpha\mu^p \quad (4)$$

$$\sigma_{i+1}^p = (1 - \alpha)\sigma_i^p + \alpha\sigma^p \quad (5)$$

where μ^p and σ^p are acquired from the elite samples. In this paper, ρ is set to 0.1, and it means that the highest 10% is considered as the elite parameter samples. This guarantees a suitable convergence velocity. α is the updating weight and is set to 0.5. This parameter is applied to smooth the trend of each parameter and guarantees a moderate learning rate. From μ_{i+1}^p and σ_{i+1}^p , the new Gaussian distribution is established and then go to step 2.

- 5) Either each parameter converges to the optimal result, i.e., $\sigma_i^p < 0.05$, or the iteration times are large enough, i.e., $i \geq 60$, the iteration stops. Then, we get the final optimal parameter setting.

TABLE I
FEATURES EXTRACTED FROM SAR IMAGES

	Symbol	Description
Preliminary Extraction	\hat{L}	The preliminary extraction of length along the principle axis
	\hat{W}	The preliminary extraction of width along the secondary axis
	\hat{H}_{\cos}	The cosine of the orientation angle extracted from the image
Sensor	θ_{\cos}	The cosine of the incidence angle at the center of the ship
	μ_{edge}	The mean NRCS of all contour pixels
Edge information	σ_{edge}	The standard deviation of all contour pixel NRCS values
	M_{edge}	The maximum NRCS of all contour pixels
Environment	μ_{env}	The mean NRCS of all environment pixels
	σ_{env}	The standard deviation of all environment pixel NRCS values
	M_{env}	The maximum NRCS of all environment pixels
Target information	N_{center}	The number of scattering centers
	μ_{center}	The mean NRCS of scattering centers
	σ_{center}	The standard deviation of scattering center NRCS values
	M_{center}	The maximum NRCS of scattering centers
	μ_{axis}	The mean NRCS of principle axis pixels
	σ_{axis}	The standard deviation of principle axis pixel NRCS values
	M_{axis}	The maximum NRCS of principle axis pixels
	μ_{BowAxis}	The mean NRCS of the bow section along the principle axis
	$\mu_{\text{MiddleAxis}}$	The mean NRCS of the middle section along the principle axis
	$\mu_{\text{SternAxis}}$	The mean NRCS of the stern section along the principle axis
	S_{target}	The sum of NRCS values of the ship target
	μ_{target}	The mean NRCS of the ship target
	σ_{target}	The standard deviation of ship target NRCS values
	$S_{\text{bow}}, S_{\text{middle}}, S_{\text{stern}}$	The sum of NRCS values of the bow, middle, and stern sections
	$\mu_{\text{bow}}, \mu_{\text{middle}}, \mu_{\text{stern}}$	The mean NRCS of the bow, middle, and stern sections
	$\sigma_{\text{bow}}, \sigma_{\text{middle}}, \sigma_{\text{stern}}$	The std of the bow, middle, and stern section NRCS values

C. Regression

1) *Feature Extraction and Fusion:* In order to get the size extraction with high accuracy, features from different sources are extracted to be used in the regression model. The features are shown with descriptions in Table I. Based on the radiometrically calibrated data, the scattering information is extracted from the normalized radar cross section (NRCS) σ_0 of pixels. The features can be divided into the following five categories.

- 1) Motivated by [21], the preliminary extraction results, as listed in the green rectangle, contain the extraction results from the image processing stage

$$F_1 = (\hat{L} \quad \hat{W} \quad \hat{H}_{\cos}). \quad (6)$$

- 2) Motivated by [21], the important parameter of the SAR system, as listed in the yellow rectangle, refers to the incidence information

$$F_2 = (\theta_{\cos}). \quad (7)$$

- 3) Motivated by [21], the edge information is listed in the red rectangle. This information is acquired from the boundary region of the ship target

$$F_3 = (\mu_{\text{edge}} \quad \sigma_{\text{edge}} \quad M_{\text{edge}}). \quad (8)$$

- 4) The environment information, as listed in the orange rectangle, contains statistical descriptors from the environment region

$$F_4 = (\mu_{\text{env}} \quad \sigma_{\text{env}} \quad M_{\text{env}}). \quad (9)$$

The environment region refers to all nontarget pixels in the SAR ship chip, and the size of the sample is according to the size of the ship target [23]. The

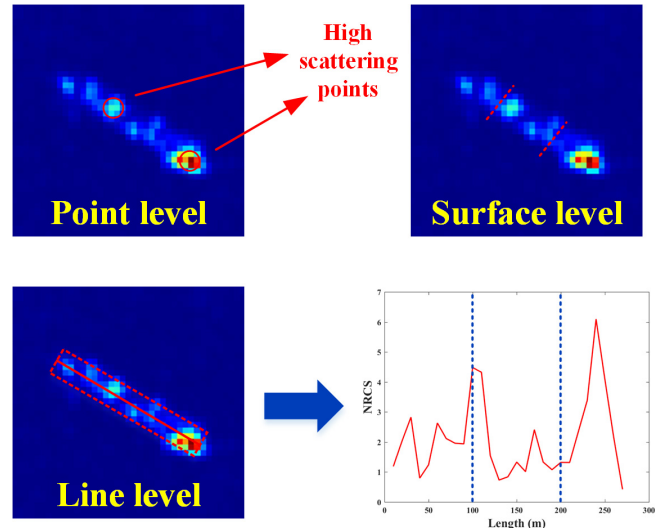


Fig. 6. Illustration of the extraction of target information at three levels.

numbers of environment pixels are different for targets of different sizes from around 2900 to 15 700 pixels in the utilized data set. For the samples the lengths of which are under 100 m, the numbers of environment pixels are around 2900. For the ship length is in the range of (100 m, 200 m] and (200 m, 300 m], the numbers of environment pixels are around 4500 and 9400. Under the condition that the length is greater than 300 m, the number of environment pixels is around 15 700.

- 5) The final information, as shown in the brown rectangle, is acquired from the target region. It contains three-level information: point, line, and surface.

The extraction of target information is shown in Fig. 6. At the point level, we extract the points with high backscattering values which are considered as the scattering centers in the ship region. The point-level information can be a typical feature for dividing various ship categories, such as bulk carriers and containers that have distinctive scattering centers. At the line level, we extract the bow-to-stern axis based on the minimum enclosing rectangle from the image processing result, as shown in the bottom left of Fig. 6. The information is essential, because most main buildings of the ships are designed to be located and symmetric along the primary axes [38]. Hence, the bow-to-stern axis NRCS information is representative for the main distinctive structure of the ship. At the surface level, the whole target region that can reflect the average information of the target is utilized. Motivated by [38], for the line level and the surface level, there are two ways of information extraction: from the whole region and from three equally divided sections of the target, referring to the bow, middle, and stern sections of the target, respectively. It is worth mentioning that the existence of aftercastles and other buildings makes the stern section generally show high backscattering; hence, the section of the ship with the highest NRCS value is regarded as the stern section, and the opposite section is regarded as the bow section [38].

$$F_5 = (F_{51} \quad F_{52} \quad F_{53}) \quad (10)$$

where

$$\begin{aligned} F_{51} &= (N_{\text{center}} \ \mu_{\text{center}} \ \sigma_{\text{center}} \ M_{\text{center}}) \\ F_{52} &= (\mu_{\text{axis}} \ \sigma_{\text{axis}} \ M_{\text{axis}} \ \mu_{\text{BowAxis}} \ \mu_{\text{MiddleAxis}} \ \mu_{\text{SternAxis}}) \\ F_{53} &= (S_{\text{target}} \ \mu_{\text{target}} \ \sigma_{\text{target}} \ S_{\text{bms}} \ \mu_{\text{bms}} \ \sigma_{\text{bms}}) \end{aligned}$$

and

$$\begin{aligned} S_{\text{bms}} &= (S_{\text{bow}} \ S_{\text{middle}} \ S_{\text{stern}}) \\ \mu_{\text{bms}} &= (\mu_{\text{bow}} \ \mu_{\text{middle}} \ \mu_{\text{stern}}) \\ \sigma_{\text{bms}} &= (\sigma_{\text{bow}} \ \sigma_{\text{middle}} \ \sigma_{\text{stern}}). \end{aligned}$$

As analyzed in Section II-A, the polarization is an important factor and the information from two polarization channels can be mutually complementary under some circumstances. Thus, in this paper, we propose to combine the scattering information from the two polarization channels together and generate the following feature vector:

$$X = (F^{\text{VH}} \ F^{\text{VV}})^T \quad (11)$$

and

$$\begin{aligned} F^{\text{VH}} &= (F_1^{\text{VH}} \ F_2^{\text{VH}} \ F_3^{\text{VH}} \ F_4^{\text{VH}} \ F_5^{\text{VH}}) \\ F^{\text{VV}} &= (F_1^{\text{VV}} \ F_3^{\text{VV}} \ F_4^{\text{VV}} \ F_5^{\text{VV}}) \end{aligned}$$

where the superscripts VH and VV indicate the polarization channels from which the features are extracted, and the superscript T denotes the matrix transpose. Since the incidence angle information is the same in the two polarization channels, F_2^{VV} is not included in F^{VV} .

2) *Nonlinear Regression*: Not only the feature extraction but also the regression model selection is essential to achieve high accuracy for the geometric parameter extraction. A suitable regression model is able to reflect the inner relationship between the influential factors and the geometric parameters. Research [21] has demonstrated that the linear regression model is an applicable model under the assumption of the linear inner relationship. This paper proposes that the nonlinear inner relationship is a more reliable assumption.

Studies have been carried out to explore the relationship between the ship size and its scattering information. An empirical formula [19] is $\sigma = 52f^{1/2}D^{3/2}$, where σ and f denote the radar cross section and the radar frequency, respectively, and D denotes the displacement of the ship reflecting the ship size. The displacement of a ship is its weight and measured by the water its hull displaces. Then, a modified formula between the ship length and its scattering information for a certain type of fleet [18], [39] was presented as $L = (\sigma_{\text{ship}}/(0.08 \times R(\theta)))^{3/7}$, where σ_{ship} and L denote the radar cross section and the length of the ship, respectively, $R(\theta)$ is defined as $R(\theta) = 0.78 + 0.11\theta$, and θ denotes the incidence angle. Up to now, sound and unified solutions toward this problem have not been given yet. However, studies propose that the nonlinear inner relationship between the ship size and the system parameter or the scattering information is a reliable assumption. In addition, the role of the orientation angle in the regression of this paper should be nonlinear, and this

is analyzed in Section II-A and verified in Section III-C. Therefore, here we explore the nonlinear inner relationship between the ship size and the influential factors and propose to use the nonlinear regression model.

For the regression problem, when the value of the loss function decreases to a stable stage with little change, the loss function converges to the final value and the regression model is obtained. For the regression model result, the balance between underfitting and overfitting needs to be considered. The underfitting [40] model may lack accurate parameters or terms which are supposed to appear, for example, fitting nonlinear training data via a linear model. The underfitting model proposes a poor prediction capability. On the other hand, overfitting usually occurs when the regression model is very complex and describes the random error or noise which should be ignored in the model. The overfitting [41] occurs when the result model corresponds too closely to some particular data points and lacks generalization ability toward the testing data set. Therefore, we should select a suitable regression model that is capable of capturing the patterns under the training data sets, as well as performing well in the testing data sets. To avoid underfitting and overfitting, choosing a suitable regression model is the first step. In addition, some implementations are indispensable, such as regularization, the split of the training and testing data sets, and cross validation.

Considering the various relationships of the geometric parameters and multiple factors, the gradient boosting [42], [43] is utilized in this paper. The gradient boosting is an effective and efficient method, allowing for the optimization of arbitrary differentiable loss functions. This method establishes an additive model in a forward stagewise manner, and in every stage, a regression tree is fit to the training data on the negative gradient according to the utilized loss function. The additive model makes the gradient boosting that has the capability of handling data of mixed types and modeling complex functions. It is suitable for the heterogeneous feature data we face in this paper, considering five categories of features from different sources and different polarization channels for size regression.

$F(x)$ is the function that maps x to y . In this method, boosting approximates $F(x)$ by an additive model, which is established as

$$F(x) = \sum_{m=1}^M \gamma_m h_m(x) \quad (12)$$

where $h(\cdot)$ is the regression tree as the basis function, and γ is the step length.

In the gradient boosting, the above additive model is realized in a forward stagewise manner. The iteration is described as

$$F_m(x) = F_{m-1}(x) + \gamma_m h_m(x) \quad (13)$$

where m denotes the m th iteration.

For the m th iteration, the regression tree $h_m(x)$ is fit by the negative gradient as follows:

$$\left\{ \left(x_i, -\frac{\partial \mathcal{L}(y_i, F_{m-1}(x_i))}{\partial F_{m-1}(x_i)} \right) \right\}_{i=1}^N \quad (14)$$

where $\mathcal{L}(\cdot)$ denotes the loss function, which is chosen as the square loss in this paper, N denotes the number of data samples, and the step length is chosen to minimize the total loss as

$$\gamma_m = \arg \min_{\gamma} \sum_{i=1}^N \mathcal{L}(y_i, F_{m-1}(x_i) + \gamma h_m(x_i)). \quad (15)$$

Utilizing the shrinkage parameter v [43] to control the learning rate, (13) is modified as follows:

$$F_m(x) = F_{m-1}(x) + v \gamma_m h_m(x) \quad (16)$$

where the parameter v is set to 0.1 in this paper for a moderate learning procedure. More detailed information about the gradient boosting regression can be found in [42]–[44]. In this paper, the gradient boosting regression is implemented by scikit-learn [45].

III. EXPERIMENTS AND RESULTS

This section presents the performance of the size parameter extraction. The parameters optimized from the cross-entropy method are used in the image processing stage. The preliminary extraction achieves a good performance, 7.73% (14.93 m) and 36.77% (10.64 m) for length and width, respectively. Based on the preliminary extraction results, the final size parameter retrieval by the nonlinear regression is presented with both visual presentation and numerical evaluation. The elaborate extraction achieves a subpixel accuracy level, 4.66% (8.80 m) and 7.01% (2.17 m) for length and width, respectively.

A. Data Sets and Performance Evaluation

Here, the OpenSARShip [23] is selected as the data set for the following reasons. First, this data set provides trustworthy ground truth, where a large volume of samples have been integrated with the AIS messages. Second, the focus on the ship chip ensures the full attention on the geometric parameter extraction which is the key problem in this paper. In the data set, the SAR ship chip is acquired from the original SAR image with the assistance of the AIS message and the manually extracted information [23].

We use 1850 samples as the experimental data set, which are from the IW mode and the GRD products of Sentinel-1 with VH and VV dual polarizations. These products are the main products for the harbor surveillance of Sentinel-1 with a large volume of ship samples. These samples are acquired from 22 scenes in recent years, covering 5 typical ports with intense marine traffic: Shanghai Port (China), Shenzhen Port (China), Tianjin Port (China), Yokohama Port (Japan), and Singapore Port (Singapore). The resolution is about 20 m, and the pixel spacing is 10 m. The whole experimental samples cover a large range of geometric size from 92 m to 399 m and 6 m to 65 m for length and width, respectively.

In this paper, two evaluation criteria are selected to assess the performance quantitatively: the error, which is composed of the relative error and the absolute error, and the correlation coefficient between the estimation and the ground truth.

TABLE II
OPTIMIZED PARAMETERS FOR THE IMAGE PROCESSING STAGE
ACHIEVED BY THE CROSS-ENTROPY METHOD

Parameters	VH	VV
ρ_{th}	0.4974	0.4620
s_{rg}	1.0617	1.0258
s_{az}	1.0215	1.0365
ρ_{PA}	0.7333	0.5008
ρ_{SA}	0.6087	0.5751

- 1) The relative error for one sample is defined as

$$\frac{|\hat{G}(n) - G(n)|}{G(n)} \times 100\% \quad (17)$$

where $\hat{G}(n)$ and $G(n)$ denote the estimated geometric parameter, i.e., length or width, and its ground truth from the AIS message for the n th sample, respectively.

- 2) The absolute error for one sample is defined as

$$|\hat{G}(n) - G(n)|. \quad (18)$$

- 3) The correlation coefficient is defined as

$$r = \frac{1}{N-1} \sum_{n=1}^N \left(\frac{\hat{G}(n) - \mu_{\hat{G}}}{\sigma_{\hat{G}}} \right) \left(\frac{G(n) - \mu_G}{\sigma_G} \right) \quad (19)$$

where N is the number of the experimental samples, and μ and σ are mean and standard deviation of the samples, extracted or ground truth ones, respectively. The correlation coefficient measures the linear correlation between the geometric estimation and the ground truth. The higher r is, the closer the geometric estimation is to the ground truth.

B. Preliminary Extraction Results

In this section, we first present the optimized parameters acquired from the cross-entropy method. Second, the preliminary length and width estimation results extracted from the image processing stage with the optimized parameters are presented both numerically and visually. Third, the effects introduced in Section II-A are analyzed based on the preliminary results.

1) *Results of Parameter Optimization*: Here, the convergence procedure in the cross-entropy method is shown in Fig. 7. Under the condition that the evaluation function decreases to its stable value with little change, the parameter setting is obtained from the cross-entropy method, as presented in Table II. From Fig. 7, a remarkable decrease and a low value with little change can be observed, which illustrates the convergence procedure of the cross-entropy method. From Table II, the parameters include ρ_{th} in the binarization operation, and s_{rg} , s_{az} , ρ_{PA} , and ρ_{SA} in the refinement of the binary result. Their definitions can be found in Section II-B.

In addition, the optimized parameters are slightly different in the two polarization channels, suggesting the different properties the two polarization channels possess. In the image processing stage, the optimized parameters acquired from the

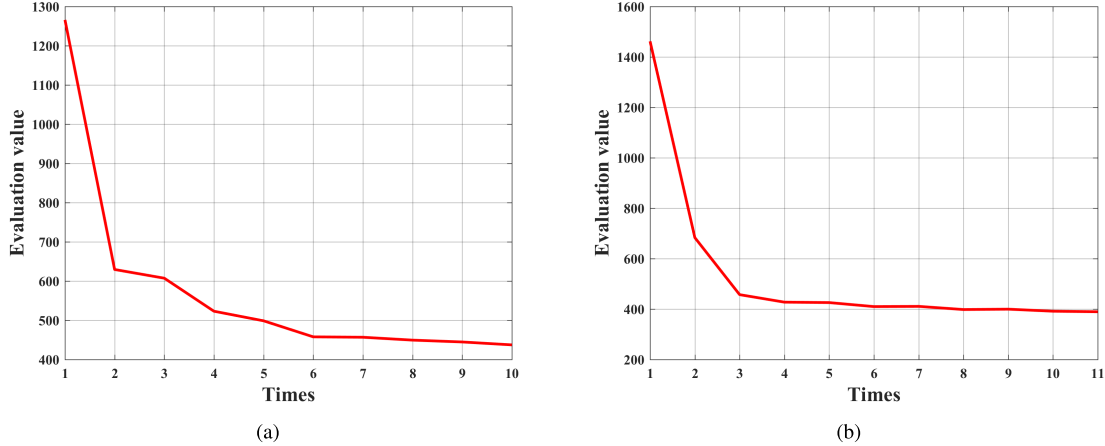


Fig. 7. Convergence procedure of the evaluation function in the cross-entropy method. (a) Convergence procedure in the VH polarization. (b) Convergence procedure in the VV polarization.

TABLE III
PRELIMINARY EXTRACTION RESULTS

	Relative error (%)		Absolute error (m)	
	Length	Width	Length	Width
VH	8.13	32.43	15.63	9.77
VV	7.33	41.10	14.22	11.51
Average	7.73	36.77	14.93	10.64

cross-entropy method facilitate the stage to achieve its optimal performance.

2) *Results of Preliminary Extraction:* After applying the optimized parameter setting acquired from the cross-entropy method to the image processing stage, the performance of the preliminary extraction is presented in Table III and Fig. 8.

From Table III, we can observe the following performance. The mean errors on average are 7.73% (14.93 m) and 36.77% (10.64 m) for length and width estimations, respectively. For the length estimation, the mean relative errors of the two polarizations are both under 10% and the mean absolute errors are close to the pixel spacing, i.e., 10 m. For the width estimation, though the mean absolute errors are close to the pixel spacing, the performances are worse than those of the length estimation. Specifically, since the ship width is much smaller than the length naturally, the ambiguities from the SAR signatures have much more influence in the width extraction. In the performance description, mean denotes the mean performance of samples, and average denotes the average performance of the two polarization channels.

Fig. 8 shows the preliminary extraction performance visually. In Fig. 8, the black line indicates that the estimation equals the ground truth reported by the AIS message. r is the correlation coefficient, as defined in Section III-A. From Fig. 8, the correlation coefficients of the length extraction are 0.92 and 0.93 for the VH and VV polarizations, respectively. The length estimation reaches relatively good agreement with the ground truth for the two polarizations. However, the width

estimation does not reach such good agreement, and this is consistent with the observations from Table III and the related studies [17], [21].

The whole experimental process has been carried out for more than 10 times. Fig. 9 shows the chip examples of representative cases in the experiments. Fig. 9(a) shows an ideal case. First, the binarization removes the noise points to a large degree. In addition, the following refinement eliminates the outliers out of the ship target. The estimated size is close to the ground truth. Fig. 9(b) and (c) shows the representative cases of complicated cases. Fig. 9(b) shows the phenomenon of strong sidelobes. The binarization with suitable parameters suppresses the undesirable effects at the first stage. Next, in the procedure of refinement, the morphology operations and the delineation technique further erase the noise points with the assistance of the parameter setting optimized via the cross-entropy method. The situation of separated ship parts is shown in Fig. 9(c). Though the image processing separates the ship signature in the image, the calculation based on the terminal locations connects the divided parts actually, as shown in the third figure of Fig. 9(c).

Considering that the performance of ship size extraction from SAR imagery is largely limited by the product resolution, the related research using the products of similar resolution is chosen for comparison. Based on the mathematical morphology operations, Stasolla and Greidanus [17] utilize 127 ship samples of Sentinel-1 IW products to estimate their sizes. The mean relative error and the mean absolute error of the estimation are 16% (30 m) and 37% (11 m) for length and width, respectively. Employing the image processing with the optimized parameter setting, Tings *et al.* [21] use 97 samples of TerraSAR-X ScanSAR images and the correlation coefficients between the estimation and the ground truth are 0.59 and 0.32 for length and width, respectively.

Comparing the results of this paper with the related research, for the length estimation, the error of this paper, 7.73% (14.93 m), is around half of that of the mathematical morphology method, 16% (30 m). In addition, the correlation coefficient, 0.93 on average, of this paper is higher than

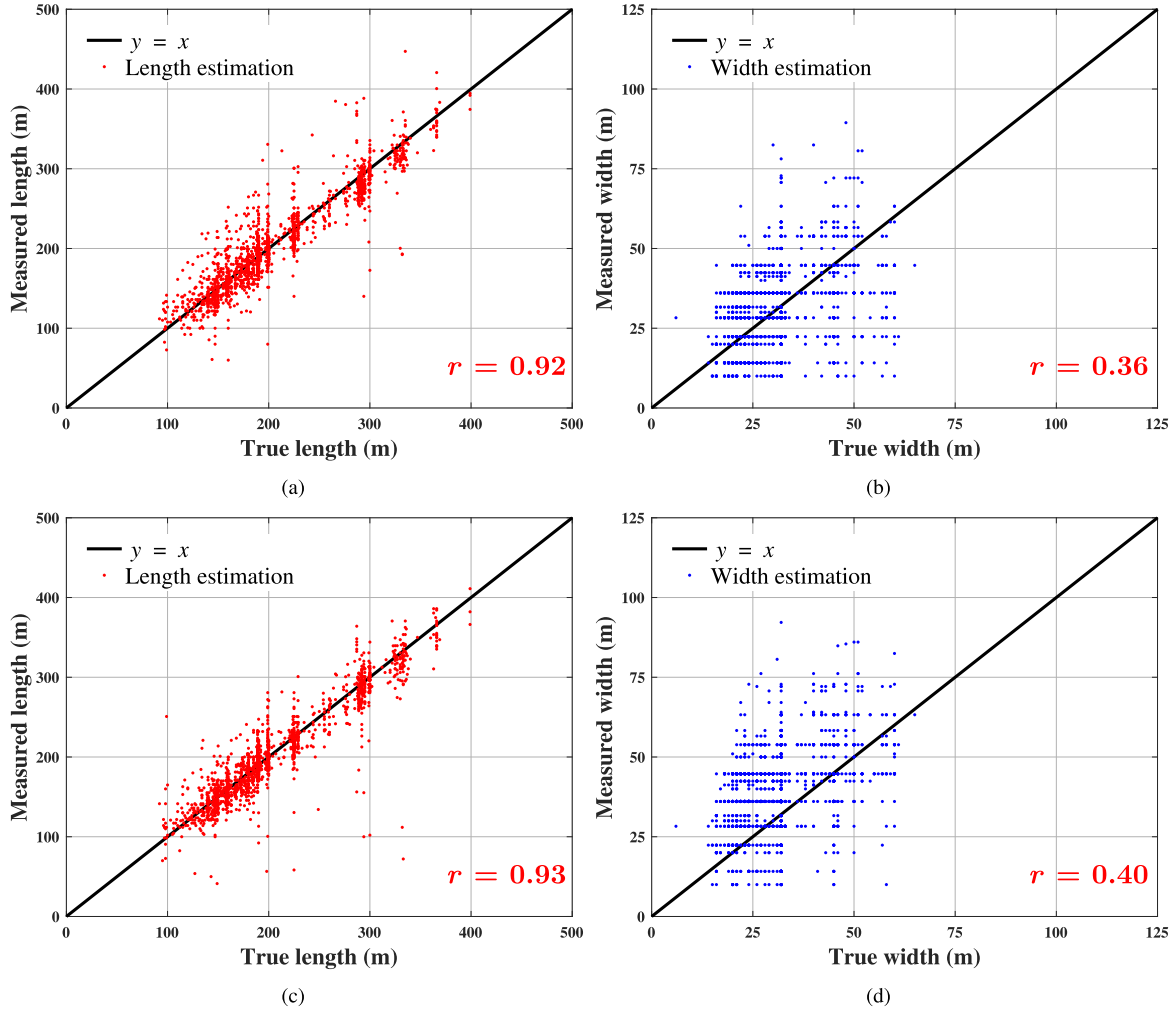


Fig. 8. Preliminary extraction results from SAR images. (a) and (c) Relationships of the measured length and the true length for the VH and VV polarizations, respectively. (b) and (d) Relationships of the measured width and the true width for the VH and VV polarizations, respectively.

the result of [21], 0.59, indicating that there is a higher agreement between the estimation and the ground truth. For the width estimation, the error of this paper, 36.77% (10.64 m), is smaller than the mathematical morphology method, 37% (11 m), and the correlation coefficient, 0.38 on average, is higher than the result of [21], 0.32. From the aspects of the error and the correlation coefficient, the image processing stage of the proposed method provides a better performance than the existing research for a more suitable design in this stage. For the width estimation, the performance is slightly better, and this will be much improved after the nonlinear regression.

3) *Analyses of Preliminary Extraction Results:* The size extraction is influenced by multiple factors that are introduced in Section II-A. Based on the preliminary extraction results, the typical factors are selected and analyzed, aiming to verify the analyses of influential factors in Section II-A. The length extraction is selected as a representative to analyze the influential factors.

1) *Analysis on the Ship Condition:* The ship condition, including its velocity and orientation, has impacts on the size extraction. The mean and the standard deviation of the relative error in the length extraction are shown

in Fig. 10 with respect to the change of orientation. The orientation angle measures the ship orientation with respect to the azimuth direction, as shown in Fig. 11. The orientation angle does not distinguish between the bow and the stern of one ship, and hence, the range of the orientation angle is $(-90^\circ, 90^\circ]$. From Fig. 10, the error change can be observed with the change of the orientation. The errors are higher and spread more widely when the orientation angles are closer to 0° . Several factors induce this phenomenon: smearing caused by the ship velocity component in the azimuth direction, unequal resolutions after image formation ($5 \text{ m} \times 20 \text{ m}$ for range and azimuth directions, respectively; the lower resolution enlarges the errors in the azimuth direction), and so on. We consider that ship motion together with lower resolution in azimuth contributes greatly to this phenomenon. In addition, the two polarization channels also have relatively different performances with respect to the ship motion in the experiments. In general, in the range of $(-30^\circ, 30^\circ]$, where the extraction is more likely to be affected by the ship motion, the errors of the VH polarization are higher than those of the VV polarization. This is shown in Fig. 10.

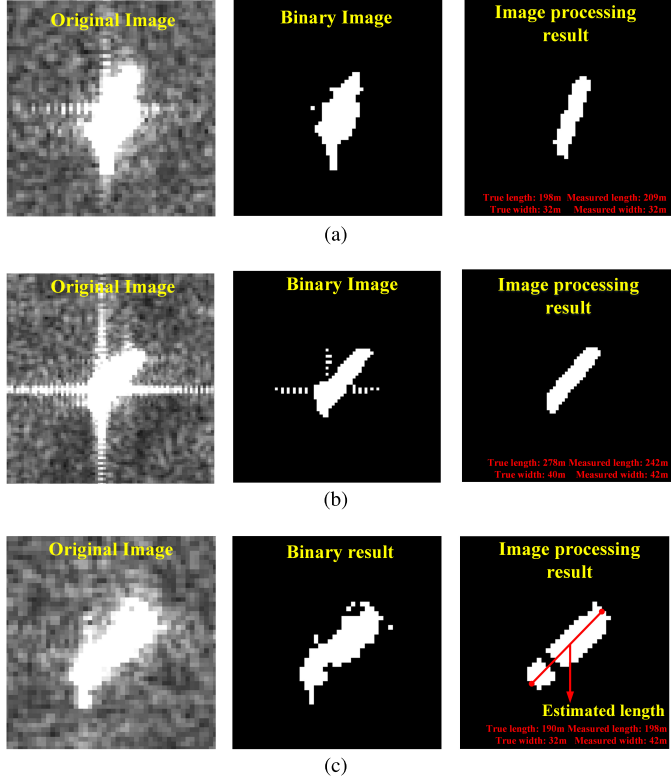


Fig. 9. Preliminary extraction results of typical SAR ship chips. (a) Ideal case. (b) Condition that the sidelobe is strong. (c) Condition that the ship target is separated into more than one part.

2) *Analysis on the Ship Type*: Different ship types have different performances. With the information provided by the MarineTraffic Website [46], the OpenSARShip contains the elaborate type message for each sample. In this paper, the data set covers five typical ship types: tanker, bulk carrier, container, general cargo, and other, which have various superstructures. The tanker is a typical ship designed to transport liquids in bulk. The bulk carrier is used for transporting bulk cargo items and, generally, has large boxlike hatches on the deck. The container is a type of cargo that carries all of its loads in truck-size containers. The general cargo is a general type of cargo that locates its goods in packages, bags, or containers. The other type includes the dredger, the passenger ship, and some unspecific-type samples. The mean relative errors for the above five types are listed in Table IV. The former four types have relatively good performances, while the fifth type has the worst performance due to the large diversities of samples within this type. Considering the differences among ship types reflected on the scattering information of targets, the size estimation will be improved by the regression.

From the above-mentioned analyses, some of the undesirable effects still exist in the preliminary results. These effects are reflected in the SAR signatures, as analyzed in Section II-A. Therefore, the implementation of a suitable regression model as well as dual-polarization information fusion is essential to further improve the extraction

TABLE IV
RELATIONSHIP BETWEEN THE MEAN RELATIVE ERROR (%)
IN THE LENGTH EXTRACTION AND THE SHIP TYPE

	Tanker	Bulk carrier	Container	General cargo	Other type
VH	9.23	6.78	7.03	9.60	16.33
VV	8.93	6.24	6.71	8.30	15.76

performance, and the regression results are analyzed in Section III-C.

It is worth mentioning that there are some parameters that are decided empirically. In the cross-entropy method, the initial values of μ and σ , the number of parameter sets N in each iteration, the ratio for the elite sample number ρ , the weights ω_L and ω_W , the updating weight α , and the stopping criteria are selected manually. As described in Section II-B3 in detail, these empirical parameters are set to guarantee a sufficient search coverage, a moderate convergence speed, and a good performance for the cross-entropy method. The performance is relatively robust if parameters change within certain ranges.

C. Regression Results

In the regression stage, we employ the dual-polarization information fusion and the gradient boosting regression to exploit the nonlinear inner relationship between the influential factors and the size parameters. Here, we present the regression performance in detail. First, we present the extraction performance improvement after the regression. Second, we demonstrate the improvement after the dual-polarization information fusion. Third, the performance of the nonlinear regression model is compared with those of the linear models. Finally, the influential factors represented in the regression model are selected and analyzed;

70% of the whole data set is divided into the training data set randomly and the left 30% is for the testing. To avoid the overfitting problem, the cross validation is also implemented in the data set. The details of the cross validation can be found in [47].

Considering that the linear regression model is a simple model which has been proven to be useful [21], the linear regression model is implemented as well as its shrinkage modifications for performance comparison.

1) *Improvement After the Regression*: Comparing the preliminary extraction results in Table III and the regression results in Table V, the performance improvement can be observed. Even for the simple linear regression model, the width estimation error decreases to 9.09% (2.87 m) and 9.47% (2.87 m) for the VH and VV polarizations, respectively. In addition, the length estimation error decreases to 6.53% (12.47 m) and 6.84% (12.84 m) for the VH and VV polarizations, respectively. The results show that the regression stage is effective especially for the width estimation. The geometric parameter estimations reach similar performances in the VH and VV polarizations. In order to achieve higher performances, the fusion of the dual-polarization information

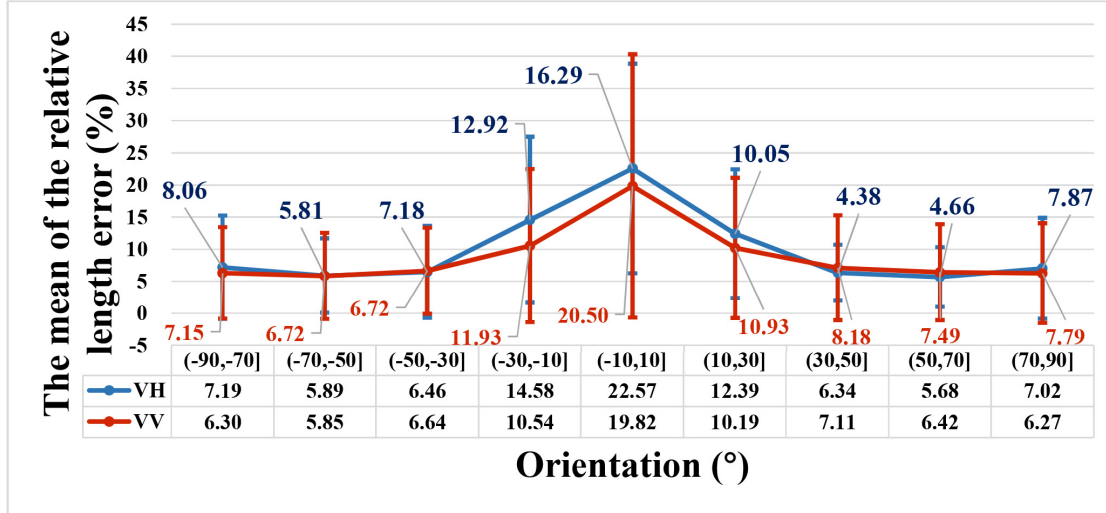


Fig. 10. Quantitative analysis of the influence of the orientation angle in the length extraction in the preliminary extraction results.

TABLE V
PERFORMANCE COMPARISON OF SINGLE-POLARIZATION FUSION AND DUAL-POLARIZATION FUSION

		Relative error (%)		Absolute error (m)	
		Length	Width	Length	Width
Linear regression	VH	6.53	9.09	12.47	2.87
	VV	6.84	9.47	12.84	2.87
	Fusion	5.78	8.54	11.02	2.68
Gradient boosting regression	VH	5.57	7.96	10.53	2.46
	VV	5.68	7.82	10.71	2.41
	Fusion	4.66 (3.54)	7.01 (5.43)	8.80 (6.73)	2.17 (1.61)

and the exploitation of the nonlinear inner relationship are essential.

2) *Dual-Polarization Fusion*: Table V shows the performance comparison of single-polarization fusion and dual-polarization fusion. For the linear regression model, the length estimation error after the fusion decreases by 0.75% (1.45 m) and 1.06% (1.82 m) compared to those with the VH and VV polarizations, respectively and for width, 0.55% (0.19 m) and 0.93% (0.19 m), respectively. For the nonlinear regression model, the length estimation error after the fusion decreases by 0.91% (1.73 m) and 1.02% (1.91 m) compared to those with the VH and VV polarizations, respectively, and for width, 0.95% (0.29 m) and 0.81% (0.24 m), respectively. By percentage, the extraction errors after the fusion are reduced to approximately 80%–90% of those with single polarizations. Both the linear and nonlinear regression models verify that the dual-polarization information should be fused and the size extraction performance is improved.

In addition, the performance of the dual-polarization fusion on the training data set for the nonlinear regression is presented in parentheses. The small difference in the performances of the training and testing data sets indicates that the samples are uniformly distributed in the two data sets. The undesired

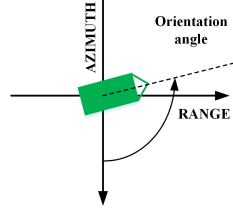


Fig. 11. Illustration of the orientation angle.

phenomena of regression described in Section II-C2, underfitting and overfitting, do not appear here.

3) *Nonlinear Versus Linear*: Here, we present the performance of the gradient boosting regression that exploits the nonlinear inner relationship between the influential factors and the size parameters. For comparison, the linear regression model and its two shrinkage modifications are implemented. The loss function of the linear regression is defined as the square loss and the same as that of the nonlinear regression. For the ridge method [48], the ℓ_2 -norm of the parameters is used as the regularizer and added to the loss function. For the lasso method [48], the ℓ_1 -norm of the parameters is used as the regularizer and added to the loss function. The shrinkage modifications address the shortcomings of the traditional linear regression method via the introduction of the regularizers. They can show their own advantages in the situations they are suitable for. The results of the three linear methods and the gradient boosting method are listed in Table VI.

For the linear regression results in Table VI, the best results are provided by the linear regression with ridge regularization. By comparison, the linear regression with lasso regularization provides the worst performance, and this suggests that in order to get high accuracy, it is not the best choice to delete the less important parameters.

As listed in Table VI, the gradient boosting regression provides an evidently improved performance. By percentage, the extraction errors of the nonlinear regression are reduced

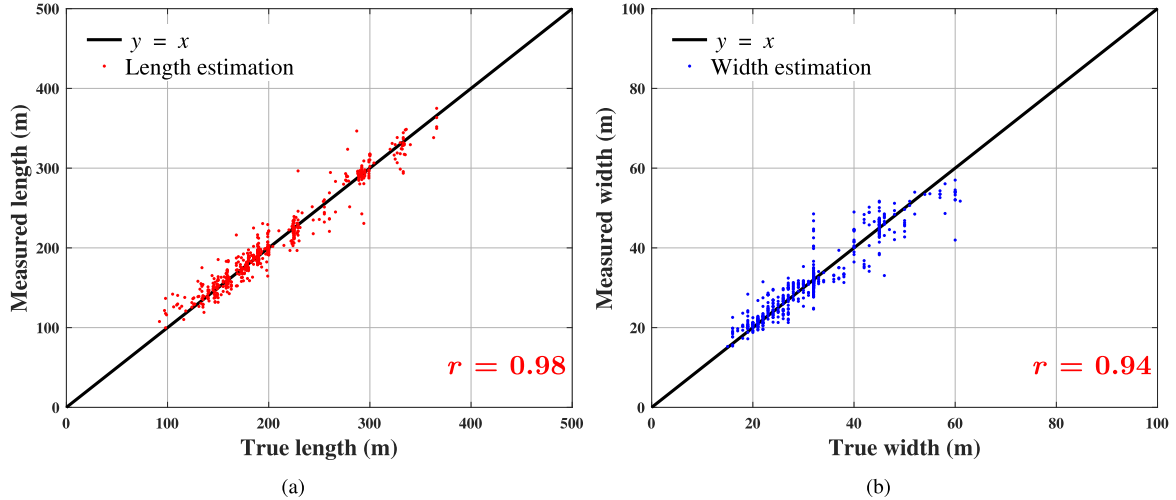


Fig. 12. Final size extraction after the nonlinear regression. (a) Relationship of the length estimation and the true length. (b) Relationship of the width estimation and the true width.

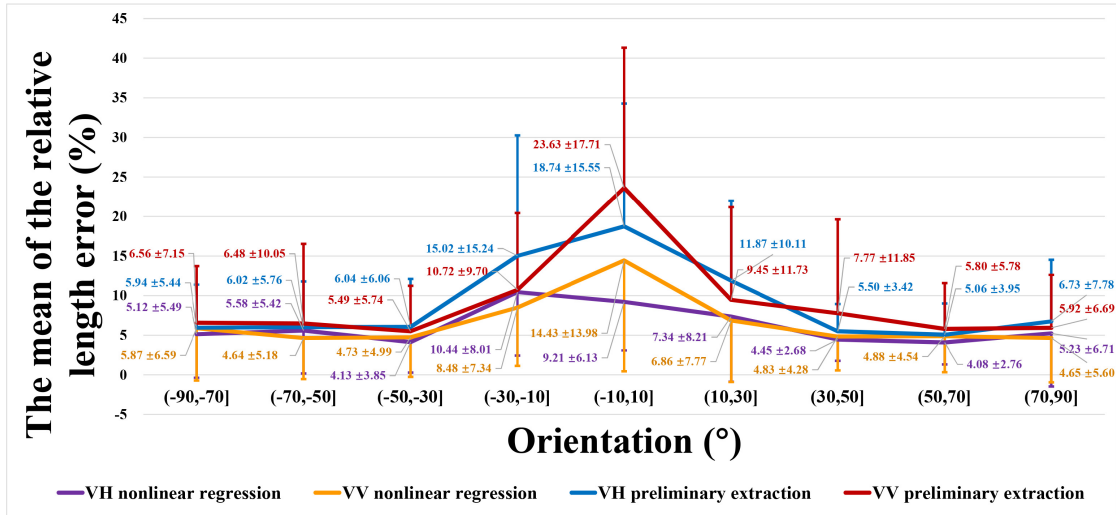


Fig. 13. Quantitative analysis of the influence of the orientation angle in the length extraction after the regression.

TABLE VI
PERFORMANCE COMPARISON OF THE LINEAR AND
NONLINEAR REGRESSION MODELS

	Relative error (%)		Absolute error (m)	
	Length	Width	Length	Width
Traditional linear	5.78	8.54	11.02	2.68
Linear with Lasso	5.82	9.02	11.07	2.81
Linear with Ridge	5.70	8.51	10.89	2.68
Gradient boosting	4.66	7.01	8.80	2.17

to approximately 80% of those of the linear regressions for length and width. In addition, the mean absolute errors are pushed under one pixel spacing, i.e., 10 m, for the length as well as the width estimation.

Fig. 12 shows the size extraction performance of the nonlinear regression visually. As the same as in Fig. 8, the black line indicates that the estimation equals the ground truth, and r is the correlation coefficient. Compared with the preliminary extraction results in Fig. 8, there is an evident improvement especially in the width estimation. The correlation coefficients r are 0.98 and 0.94 for the length and width estimations, respectively, indicating that both the length and the width estimations agree well with their respective ground truths after the nonlinear regression.

Here, we compare the results of this paper with the regression performance of Tings *et al.* [21], where the correlation coefficients r are 0.76 and 0.66 for the length and width estimations, respectively. The improvements are 0.22 and 0.28 for the length and width estimations, respectively, due to the dual-polarization fusion and the nonlinear regression employment.

In this section, the experiments show that with the fusion of the dual-polarization information and the employment of the nonlinear regression method, the size extraction performances

are improved and the errors are pushed under one pixel. This verifies the effectiveness of the proposed design.

4) Analyses of Influential Factors in Regression: Further assessment is presented based on the regression results. Here, the length estimation is chosen as a representative to analyze the influential factors. On one hand, the influence of the orientation angle is selected to analyze the use of the regression model from a different perspective, instead of the error and the correlation coefficient. On the other hand, we rank the factors with respect to their relative importances.

a) Analysis of orientation: The nonlinear regression results together with the preliminary extraction results of the testing data set are shown in Fig. 13 with respect to the orientation change. In Fig. 13, the red and yellow lines represent the preliminary extraction and nonlinear regression results for the VV polarization, respectively, and the blue and purple lines represent the preliminary extraction and nonlinear regression results for the VH polarization. From Fig. 13, we can make two observations. First, in the ranges of $(-90^\circ, -50^\circ]$ and $(50^\circ, 90^\circ]$, there is a slight decrease in the estimation error for the nonlinear regression. Second, in the range of $(-50^\circ, 50^\circ]$, i.e., close to the azimuth direction, the decrease in the mean and the standard deviation of the relative error is remarkable. Especially, in the range of $(-10^\circ, 10^\circ]$, nearly half of the errors are reduced.

Specifically, we further analyze the related parameters of the smearing. Considering that the ship motion is generally along its orientation, the orientation factor is chosen. Here, the partial dependence [43] is utilized to interpret the regression model. The partial dependence represents the dependence between the factor and the response based on the fit regression model. The partial dependence of a certain factor can be interpreted as the expected target response in the model, marginalizing over all other factors. This partial dependence reflects the influence of a certain factor in the model result. The detailed information about the partial dependence can be found in [43]. The partial dependences of the 3rd factor, i.e., the cosine of the orientation angle extracted from the VH polarization, and the 35th factor, i.e., the cosine of the orientation angle extracted from the VV polarization, are shown in Fig. 14. A drastic change of the partial dependence can be observed, if the cosine value of the orientation is located in the range of $[0.8, 1]$, i.e., the range indicating the orientation is along the azimuth direction. Taking Fig. 10 into consideration as well, there are several factors that may induce this phenomenon that the estimation errors are higher if the orientations are along the azimuth direction. We consider that the ship motion and the unequal resolution play the major roles. If the ship motion is along the azimuth direction, the azimuth component of the velocity is higher. This higher velocity component leads to the greater smearing in the SAR image, resulting to the larger length estimation in the image processing stage. Therefore, the sharp negative responses from both the 3rd factor and the 35th factor are employed within the nonlinear regression model to eliminate the influence of the smearing. From the above observations, the gradient boosting regression based on the extracted factors deliberately suppresses the larger errors in the situation that the orientations are along the azimuth direction.

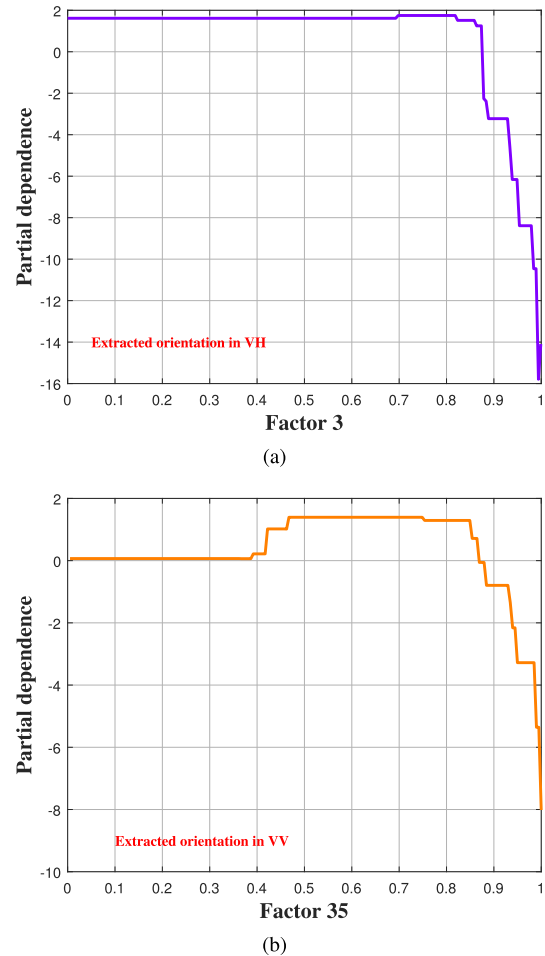


Fig. 14. Partial dependences of factors. (a) Partial dependence of the third factor, i.e., the cosine of the orientation angle extracted from the VH polarization. (b) Partial dependence of the 35th factor, i.e., the cosine of the orientation angle extracted from the VV polarization.

These results verify that the relationship of the length and the orientation angle in the regression model should be nonlinear.

b) Ranking of factors: Based on the results of the gradient boosting regression, we rank the contributions of the influential factors in the regression model. Here, the relative importance is used as the prediction contribution of the factor. The detailed information of the relative importance can be found in [43].

The relative importances of all factors in the gradient boosting regression for the VH and VV polarizations as well as the dual-polarization fusion are shown in Fig. 15. The factor is represented by its sequence number. In the regression models of both the VH and VV polarizations, there are 32 factors, and the sequence number is from 1 to 32. In the regression model of the dual-polarization fusion, there are 63 factors, and the sequence number is from 1 to 63. For the VH and VV polarizations, top five factors are regarded as the main factors, as shown in Fig. 15(a) and (b). For the dual-polarization fusion, top 10 factors are regarded as the main factors, as shown in Fig. 15(c).

From Fig. 15, the preliminary extraction result, the orientation angle, and the scattering factors are the main factors with

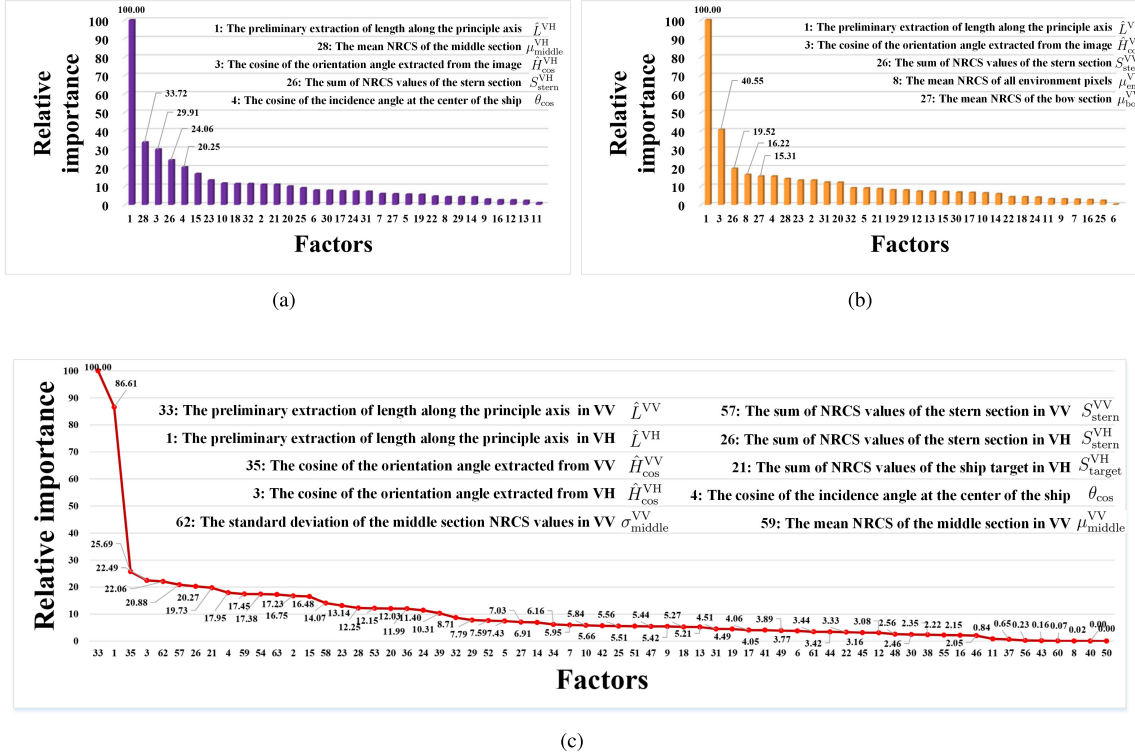


Fig. 15. Relative importances of the factors in the regressions. (a) and (b) Relative importances in the regressions of the VH and VV polarizations, respectively. (c) Relative importances in the regression of dual-polarization fusion.

major influences in the regression. The preliminary extraction result is the most important factor in the regression, and this is understandable. The orientation angle plays an important role in the regression as well, and this is consistent with the aforementioned analysis. The system factor, i.e., the incidence angle, is also an important factor which cannot be ignored. As for the target scattering factors, they are essential too. Specifically, the scattering factors of the three sections, i.e., bow, middle, and stern, are important in size extraction. The reasons are as follows. First, in the real scenarios, the existence of aftercastles, which usually cause strong backscattering, makes the stern section nonignorable. Second, for the middle section of the ship, the centroid of the ship target, determining the extraction of both length and width directly, is usually located here. Third, the distribution of the scattering information in the three sections reflects the type of the ship, which is also influential to the size extraction, as discussed in Section III-B3.

In this section, we show that the nonlinear regression stage aims to different undesirable effects and then suppresses them. In addition, multiple influential factors have different contributions to the final results.

At the end of this section, it is worth mentioning that in the regression stage, the shrinkage parameter ν is decided empirically. According to the research in [42]–[44], ν is set to 0.1 for a moderate learning procedure. The performance of the regression is relatively robust if ν changes in a certain range.

D. Validation in Another Environmental Condition

Because of the application requirement of the OpenSARShip [23], the majority of the samples in the data set are located in the harbors of China, Asia. In order

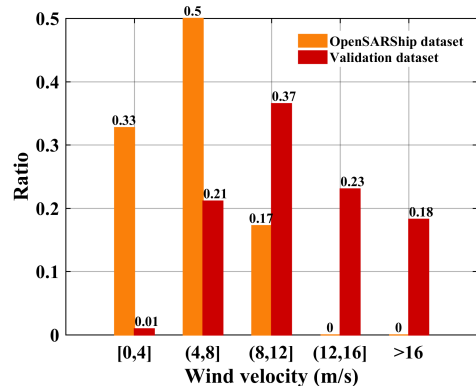


Fig. 16. Wind conditions in the representative cases of the OpenSARShip and the validation data set.

to further estimate the performance under more rigorous environmental conditions, this section presents the results in an open sea region. Ten scenes located in the North Sea are utilized as the validation data set. The length of the ship is from 84 m to 366 m, and the width is from 14 m to 60 m. In addition, the wind analyses are carried out via the SNAP software [49]. Fig. 16 shows the comparison between two representative cases in the OpenSARShip and the validation data set. From Fig. 16, an increase in the wind speed can be observed in the validation data set.

Here, the whole trained model is applied to the validation data set. In the image processing stage, the parameter values in Table II are employed. In addition, for the regression stage, the regression model described in Section III-C is

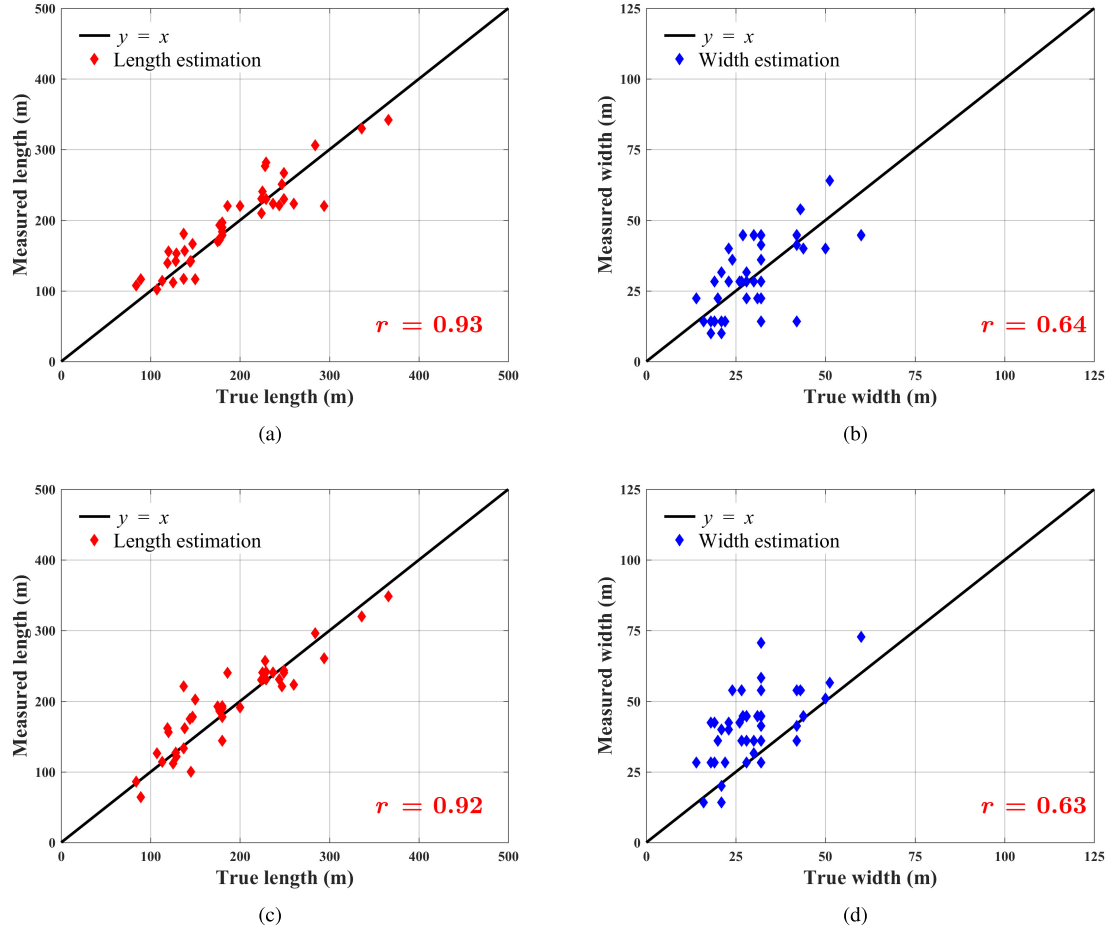


Fig. 17. Preliminary extraction from the validation data set. (a) and (c) Relationships of the measured length and the true length for the VH and VV polarizations, respectively. (b) and (d) Relationships of the measured width and the true width for the VH and VV polarizations, respectively.

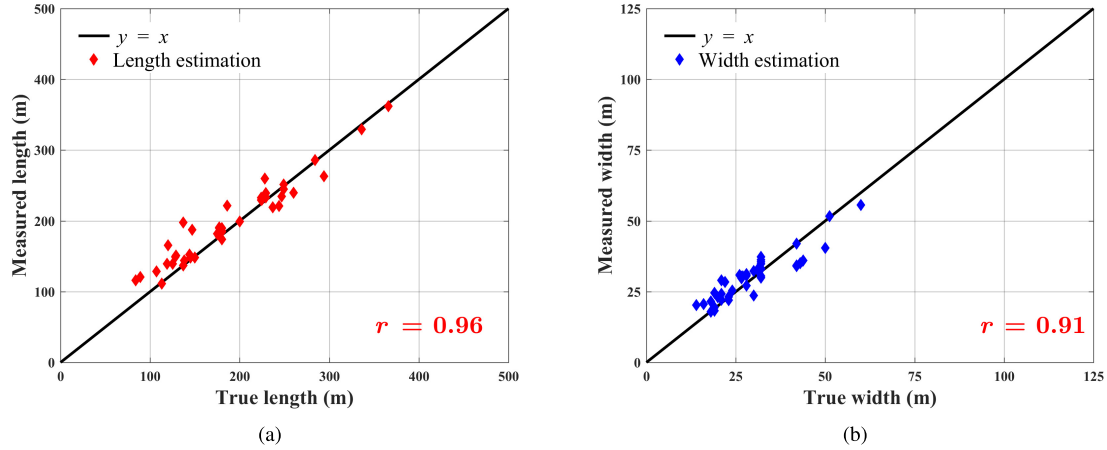


Fig. 18. Final size extraction after the nonlinear regression in the validation data set. (a) Relationship of the length estimation and the true length. (b) Relationship of the width estimation and the true width.

utilized. The results are shown in Table VII and illustrated in Figs. 17 and 18.

After the image processing, the mean errors on average for the length and width estimations are 11.75% (19.74 m) and 38.20% (10.02 m), respectively. From Fig. 17, the correlation coefficients on average for the length and width estimations are 0.93 and 0.64, respectively.

In addition, the nonlinear regression with the dual-polarization information fusion achieves the performances of 9.99% (15.03 m) and 12.88% (3.55 m) for the length and width estimations, respectively. Fig. 18 shows the regression performance. The correlation coefficients for the length and width estimations are 0.96 and 0.91, respectively.

TABLE VII
PRELIMINARY EXTRACTION AND REGRESSION RESULTS
IN THE VALIDATION DATA SET

	Relative error (%)		Absolute error (m)	
	Length	Width	Length	Width
VH (Pre)	11.21	28.70	19.40	7.94
VV (Pre)	12.29	47.70	20.07	12.09
Average (Pre)	11.75	38.20	19.74	10.02
Regression	9.99	12.88	15.03	3.55

Compared with the research [21] using the data set of the same region, the correlation coefficients indicate better performances of this paper for both the image processing stage and the regression stage.

Based on the above analyses, the performance on the validation data set confirms that the method presented in this paper is available for a relatively rough sea surface condition. In addition, the experiments further verify the applicability and the generalization capability of this procedure. It is worth noting that the performance is slight worse than the performance in the OpenSARShip, because first, the relatively rough sea surface in the North Sea worsens the estimation performance and second, the fact that the testing data set and the training data set do not have the same condition, neither the environmental condition nor the ship condition, plays a major role for the worsened performance.

IV. CONCLUSION

In this paper, we present a method of ship size extraction for Sentinel-1 images, which is composed of the image processing stage and the regression stage. In order to achieve extraction with high accuracy, considering the data characteristics of Sentinel-1 images, we propose to use the dual-polarization fusion and the nonlinear regression with the gradient boosting. The experiments on a relatively large data set show that: 1) the proposed method achieves an improved performance compared with the existing and related works. The extraction errors are pushed under one pixel; 2) the dual-polarization information fusion achieves an improved performance compared with the use of a single-polarization channel; and 3) the nonlinear regression exploits the relationship between the influential factors and the size parameters and provides a better performance than the linear regression. The experimental results verify the analyses and demonstrate that the proposed design is suitable for Sentinel-1 ship size extraction.

ACKNOWLEDGMENT

The authors would like to thank the European Space Agency for providing the Sentinel-1 data and the SNAP software. They would like to thank the editor, the associate editor, and the anonymous reviewers for their constructive suggestions and continuous encouragements. They would also like to thank Prof. J. Wang from Shanghai Jiao Tong University for the meaningful discussion on smearing caused by motion.

REFERENCES

- [1] R. Torres *et al.*, “GMES Sentinel-1 mission,” *Remote Sens. Environ.*, vol. 120, pp. 9–24, May 2012.
- [2] P. W. Vachon and J. Wolfe, “GMES Sentinel-1 analysis of marine applications potential (AMAP),” Defence Res. Develop., Canada Ottawa, Ottawa, ON, Canada, Tech. Rep. DRDC-OTTAWA-ECR-2008-218, 2008.
- [3] P. W. Vachon, J. Wolfe, and H. Greidanus, “Analysis of Sentinel-1 marine applications potential,” in *Proc. IEEE Int. Geosci. Remote Sens. Symp. (IGARSS)*, Jul. 2012, pp. 1734–1737.
- [4] J. Karvonen, “Baltic sea ice concentration estimation using Sentinel-1 SAR and AMSR2 microwave radiometer data,” *IEEE Trans. Geosci. Remote Sens.*, vol. 55, no. 5, pp. 2871–2883, May 2017.
- [5] F. Monaldo, C. Jackson, X. Li, and W. G. Pichel, “Preliminary evaluation of sentinel-1A wind speed retrievals,” *IEEE J. Sel. Topics Appl. Earth Observ. Remote Sens.*, vol. 9, no. 6, pp. 2638–2642, Jun. 2016.
- [6] L. Huang, B. Liu, X. Li, Z. Zhang, and W. Yu, “Technical evaluation of Sentinel-1 IW mode cross-pol radar backscattering from the ocean surface in moderate wind condition,” *Remote Sens.*, vol. 9, no. 8, p. 854, 2017.
- [7] D. Velotto, C. Bentes, B. Tings, and S. Lehner, “First comparison of Sentinel-1 and TerraSAR-X data in the framework of maritime targets detection: South Italy case,” *IEEE J. Ocean. Eng.*, vol. 41, no. 4, pp. 993–1006, Oct. 2016.
- [8] C. P. Schwegmann, W. Kleynhans, and B. P. Salmon, “Synthetic aperture radar ship detection using Haar-like features,” *IEEE Geosci. Remote Sens. Lett.*, vol. 14, no. 2, pp. 154–158, Feb. 2017.
- [9] R. Pelich, N. Longépé, G. Mercier, G. Hajduch, and R. Garello, “Performance evaluation of Sentinel-1 data in SAR ship detection,” in *Proc. IEEE Int. Geosci. Remote Sens. Symp. (IGARSS)*, Jul. 2015, pp. 2103–2106.
- [10] G. M. Martín, *Marine Applications of SAR Polarimetry*. Barcelona, Spain: Universitat Politècnica de Catalunya, 2007.
- [11] D. Velotto, C. Bentes, B. Tings, and S. Lehner, “Comparison of Sentinel-1 and TerraSAR-X for ship detection,” in *Proc. IEEE Int. Geosci. Remote Sens. Symp. (IGARSS)*, Jul. 2015, pp. 3282–3285.
- [12] A. Mouche and B. Chapron, “Global C-band Envisat, RADARSAT-2 and Sentinel-1 SAR measurements in copolarization and cross-polarization,” *J. Geophys. Res. Oceans*, vol. 120, no. 11, pp. 7195–7207, Nov. 2015.
- [13] M. Tello, C. López-Martínez, and J. J. Mallorqui, “A novel algorithm for ship detection in SAR imagery based on the wavelet transform,” *IEEE Geosci. Remote Sens. Lett.*, vol. 2, no. 2, pp. 201–205, Apr. 2005.
- [14] M. Messina, M. Greco, L. Fabbrini, and G. Pinelli, “Modified Otsu’s algorithm: A new computationally efficient ship detection algorithm for SAR images,” in *Proc. Tyrrhenian Workshop Adv. Radar Remote Sens. (TyWRRS)*, Sep. 2012, pp. 262–266.
- [15] M. Sugimoto, K. Ouchi, and Y. Nakamura, “On the novel use of model-based decomposition in SAR polarimetry for target detection on the sea,” *Remote Sens. Lett.*, vol. 4, no. 9, pp. 843–852, 2013.
- [16] M. Stasolla, J. J. Mallorqui, G. Margarit, C. Santamaría, and N. Walker, “A comparative study of operational vessel detectors for maritime surveillance using satellite-borne synthetic aperture radar,” *IEEE J. Sel. Topics Appl. Earth Observ. Remote Sens.*, vol. 9, no. 6, pp. 2687–2701, Jun. 2016.
- [17] M. Stasolla and H. Greidanus, “The exploitation of Sentinel-1 images for vessel size estimation,” *Remote Sens. Lett.*, vol. 7, no. 12, pp. 1219–1228, 2016.
- [18] P. W. Vachon, J. W. M. Campbell, C. A. Bjerkelund, F. W. Dobson, and M. T. Rey, “Ship detection by the RADARSAT SAR: Validation of detection model predictions,” *Can. J. Remote Sens.*, vol. 23, no. 1, pp. 48–59, 1997.
- [19] M. I. Skolnik, “An empirical formula for the radar cross section of ships at grazing incidence,” *IEEE Trans. Aerosp. Electron. Syst.*, vol. TAES-10, no. 2, p. 292, Mar. 1974.
- [20] P. W. Vachon and J. Wolfe, “Validation of ship signatures in Envisat ASAR AP mode data using AISLive: Data acquisition, processing, and analysis results,” Defence Res. Develop., Ottawa, ON, Canada, Tech. Rep. DRDC-OTTAWA-TM-2008-005, 2008.
- [21] B. Tings, C. A. B. da Silva, and S. Lehner, “Dynamically adapted ship parameter estimation using TerraSAR-X images,” *Int. J. Remote Sens.*, vol. 37, no. 9, pp. 1990–2015, 2016.
- [22] G. Hajduch, N. Longépé, J. Habonneau, and J. Y. Le Bras, “Progress in automatic ship detection and classification,” in *Proc. SeaSAR*, vol. 709, 2013, Art. no. 19.
- [23] L. Huang *et al.*, “OpenSARShip: A dataset dedicated to Sentinel-1 ship interpretation,” *IEEE J. Sel. Topics Appl. Earth Observ. Remote Sens.*, vol. 11, no. 1, pp. 195–208, Jan. 2018.
- [24] *Sentinel-1 User Handbook*, ESA, Paris, France, 2013.

- [25] F. Xu, Y.-Q. Jin, and A. Moreira, "A preliminary study on SAR advanced information retrieval and scene reconstruction," *IEEE Geosci. Remote Sens. Lett.*, vol. 13, no. 10, pp. 1443–1447, Oct. 2016.
- [26] B. H. Smith, "An analytic nonlinear approach to sidelobe reduction," *IEEE Trans. Image Process.*, vol. 10, no. 8, pp. 1162–1168, Aug. 2001.
- [27] G. Margarit, J. Mallorqui, and X. Fabregas, "Study of the influence of vessel motions and sea-ship interaction on classification algorithms based on single-pass polarimetric SAR interferometry," in *Proc. IEEE Int. Conf. Geosci. Remote Sens. Symp. (IGARSS)*, Jul. 2006, pp. 75–78.
- [28] G. Margarit, J. J. Mallorqui, J. Fortuny-Guasch, and C. Lopez-Martinez, "Exploitation of ship scattering in polarimetric SAR for an improved classification under high clutter conditions," *IEEE Trans. Geosci. Remote Sens.*, vol. 47, no. 4, pp. 1224–1235, Apr. 2009.
- [29] P. Liu and Y.-Q. Jin, "A study of ship rotation effects on SAR image," *IEEE Trans. Geosci. Remote Sens.*, vol. 55, no. 6, pp. 3132–3144, Jun. 2017.
- [30] G. Margarit, J. J. Mallorqui, J. Fortuny-Guasch, and C. Lopez-Martinez, "Phenomenological vessel scattering study based on simulated inverse SAR imagery," *IEEE Trans. Geosci. Remote Sens.*, vol. 47, no. 4, pp. 1212–1223, Apr. 2009.
- [31] C. R. Jackson and J. R. Apel, *Synthetic Aperture Radar Marine User's Manual*. Washington, DC, USA: US Department of Commerce, National Oceanic and Atmospheric Administration, National Environmental Satellite, Data, and Information Service, Office of Research and Applications, 2004.
- [32] R. Y. Rubinstein and D. P. Kroese, "The cross-entropy method a unified approach to combinatorial optimization, Monte-Carlo simulation and machine learning," in *Information Science and Statistics*. New York, NY, USA: Springer-Verlag, 2004.
- [33] C.-A. Deledalle, "Image denoising beyond additive Gaussian noise: Patch-based estimators and their application to SAR imagery," Ph.D. dissertation, Dépt. Image, Données, Signal, Télécom ParisTech, Paris, France, 2011.
- [34] X. Qin, S. Zhou, H. Zou, and G. Gao, "A CFAR detection algorithm for generalized gamma distributed background in high-resolution SAR images," *IEEE Geosci. Remote Sens. Lett.*, vol. 10, no. 4, pp. 806–810, Jul. 2013.
- [35] X. Leng, K. Ji, K. Yang, and H. Zou, "A bilateral CFAR algorithm for ship detection in SAR images," *IEEE Geosci. Remote Sens. Lett.*, vol. 12, no. 7, pp. 1536–1540, Jul. 2015.
- [36] P.-T. de Boer, D. P. Kroese, S. Mannor, and R. Y. Rubinstein, "A tutorial on the cross-entropy method," *Ann. Operat. Res.*, vol. 134, no. 1, pp. 19–67, 2005.
- [37] D. P. Kroese, S. Porotsky, and R. Y. Rubinstein, "The cross-entropy method for continuous multi-extremal optimization," *Methodol. Comput. Appl. Probab.*, vol. 8, no. 3, pp. 383–407, Sep. 2006.
- [38] G. Margarit and A. Tabasco, "Ship classification in single-pol SAR images based on fuzzy logic," *IEEE Trans. Geosci. Remote Sens.*, vol. 49, no. 8, pp. 3129–3138, Aug. 2011.
- [39] R. B. Olsen and T. Wahl, "The role of wide swath SAR in high-latitude coastal management," *Johns Hopkins APL Tech. Dig.*, vol. 21, no. 1, pp. 136–140, 2000.
- [40] B. S. Everitt and A. Skrondal, *The Cambridge Dictionary of Statistics*, vol. 106. Cambridge, U.K.: Cambridge Univ. Press, 2002.
- [41] K. P. Burnham and D. R. Anderson, *Model Selection and Multimodel Inference A Practical Information-Theoretic Approach*. New York, NY, USA: Springer-Verlag, 2003.
- [42] J. Friedman, T. Hastie, and R. Tibshirani, "Additive logistic regression: A statistical view of boosting (with discussion and a rejoinder by the authors)," *Ann. Statist.*, vol. 28, no. 2, pp. 337–407, 2000.
- [43] J. H. Friedman, "Greedy function approximation: A gradient boosting machine," *Ann. Statist.*, vol. 29, no. 5, pp. 1189–1232, 2001.
- [44] C. Li. (2016). *A Gentle Introduction to Gradient Boosting*. [Online]. Available: http://www.chenglj.io/tutorials/gradient_boosting.pdf
- [45] F. Pedregosa *et al.*, "Scikit-learn: Machine learning in Python," *J. Mach. Learn. Res.*, vol. 12, pp. 2825–2830, Oct. 2011.
- [46] MarineTraffic. (2007). *Ship List With Details and Photos*. [Online]. Available: <http://www.marinetraffic.com/en/ais/index/ships/all>
- [47] R. Kohavi *et al.*, "A study of cross-validation and bootstrap for accuracy estimation and model selection," in *Proc. Int. Joint Conf. AI*, Aug. 1995, vol. 14, no. 2, pp. 1137–1145.
- [48] J. Friedman, T. Hastie, and R. Tibshirani, "The elements of statistical learning," in *Data Mining, Inference, and Prediction* (Springer Series in Statistics), vol. 1. New York, NY, USA: Springer-Verlag, 2001.
- [49] ESA. *STEP: Science Toolbox Exploitation Platform*. Accessed: Feb. 5, 2018. [Online]. Available: <http://step.esa.int/main/>



Boying Li (S'18) received the B.Sc. degree in automation engineering from Northwestern Polytechnical University, Xi'an, China, in 2016. She is currently pursuing the Ph.D. degree with the Department of Electronic Engineering, Shanghai Jiao Tong University, Shanghai, China.

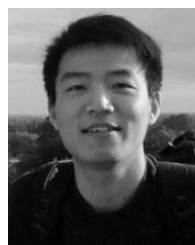
Her research interests include synthetic aperture radar image interpretation (ship detection and classification) and machine learning.



Bin Liu was born in Hengyang, Hunan, China, in 1985. He received the B.Sc. degree in information engineering and the M.Sc. and Ph.D. degrees in signal and information processing from Shanghai Jiao Tong University, Shanghai, China, in 2007, 2009, and 2015, respectively.

From 2012 to 2013, he was a Visiting Ph.D. Student with the Department of Signal and Image Processing, Telecom ParisTech, Paris, France, under the supervision of Prof. F. Tupin. From 2015 to 2018, he was a Research Assistant Professor with the Shanghai Key Laboratory of Intelligent Sensing and Recognition, Shanghai Jiao Tong University. Since 2018, he has been a Post-Doctoral Fellow with the College of Marine Sciences, Shanghai Ocean University, Shanghai, in collaboration with Prof. X. Li. His research interests include synthetic aperture radar (SAR) and polarimetric SAR image understanding and information mining, particularly spatial information analysis, segmentation and classification, multitemporal image analysis, target detection and recognition, and parameter retrievals from ocean remote sensing data.

Dr. Liu is an active Reviewer of several journals, including the *Chinese Journal of Electronics* (both in Chinese and English), the *Canadian Journal of Remote Sensing*, *Remote Sensing Letters*, the *International Journal of Remote Sensing*, the *IET Radar, Sonar & Navigation*, the *IEEE ACCESS*, the *IEEE SIGNAL PROCESSING LETTERS*, the *IEEE GEOSCIENCE AND REMOTE SENSING LETTERS*, the *IEEE JOURNAL OF SELECTED TOPICS IN APPLIED EARTH OBSERVATIONS AND REMOTE SENSING*, and the *IEEE TRANSACTIONS ON GEOSCIENCE AND REMOTE SENSING*.



Weiwei Guo received the B.Sc. and M.Sc. degrees in information and communication engineering from the National University of Defense Technology, Changsha, China, in 2005 and 2007, respectively, and the joint Ph.D. degree in information and communication engineering from the National University of Defense Technology and the Queen Mary University of London, London, U.K., in 2014.

Since 2015, he has been a Post-Doctoral Researcher with Shanghai Jiao Tong University, Shanghai, China. He has co-authored many journal publications in a number of scientific journals, including the *IEEE TRANSACTIONS ON IMAGE PROCESSING* and *Pattern Recognition*. His research interests include the areas of image and signal processing, computer vision, and pattern recognition.



Zenghui Zhang (M'13) received the B.Sc. degree in applied mathematics, the M.Sc. degree in computational mathematics, and the Ph.D. degree in information and communication engineering from the National University of Defense Technology (NUDT), Changsha, China, in 2001, 2003, and 2008, respectively.

From 2008 to 2012, he was a Lecturer with the Department of Mathematics and System Science, NUDT. He is currently an Associate Professor with the School of Electronic Information and Electrical Engineering, Shanghai Jiao Tong University, Shanghai, China. His research interests include radar signal processing and compressed sensing theory and applications.



Wenxian Yu was born in Shanghai, China, in 1964. He received the B.Sc. degree in radio measurement and control and data transmission, the M.Sc. degree in communication and electronic system, and the Ph.D. degree in communication and information system from the National University of Defense Technology (NUDT), Changsha, China, in 1985, 1988, and 1993, respectively.

From 1996 to 2008, he was a Professor with the College of Electronic Science and Engineering, NUDT, where he served as the Deputy Head of the College and the Assistant Director of the National Key Laboratory of Automatic Target Recognition. From 2009 to 2011, he was the Executive Dean with the School of Electronic Information and Electrical Engineering, Shanghai Jiao Tong University, Shanghai, where he is currently a Yangtze River Scholar Distinguished Professor. His research interests include radar target recognition, remote sensing information processing, multisensor data fusion, and integrated navigation system. He has published over 200 research papers in these areas.